PNAS RESEARCH ARTICLE | NEUROSCIENCE OPEN ACCESS

The periaxonal space as a conduit for cerebrospinal fluid flow to peripheral organs

Xinyu Li[a,b,c], Siman Wang[a,b,c], Dianjun Zhang[a,b,c], Yuliang Feng[a,b,c], Yingyu Liu[a,b,c], Weiyang Yu[a,b,c], Lulu Cui[a,b,c], Tibor Harkany[d,e], Alexei Verkhratsky[a,f,g,h,1], Maosheng Xia[i,1], and Baoman Li[a,b,c,1]

Affiliations are included on p. 11.

Edited by Maiken Nedergaard, Kobenhavns Universitet Sundhedsvidenskabelige Fakultet, Copenhagen, Denmark; received January 12, 2024; accepted September 20, 2024 by Editorial Board Member Jeremy Nathans

Mechanisms controlling the movement of the cerebrospinal fluid (CSF) toward peripheral nerves are poorly characterized. We found that, in addition to the foramina Magendie and Luschka for CSF flow toward the subarachnoid space and glymphatic system, CSF outflow could also occur along periaxonal spaces (termed "PAS pathway") from the spinal cord to peripheral organs, such as the liver and pancreas. When interrogating the latter route, we found that serotonin, acting through 5-HT_{2B} receptors expressed in ependymocytes that line the central canal, triggered Ca^{2+} signals to induce polymerization of F-actin, a cytoskeletal protein, to reduce the volume of ependymal cells. This paralleled an increased rate of PAS-mediated CSF redistribution toward peripheral organs. In the liver, CSF was received by hepatic stellate cells. CSF efflux toward peripheral organs through the PAS pathway represents a mechanism dynamically connecting the nervous system with the periphery. Our findings are compatible with the traditional theory of CSF efflux into the glymphatic system to clear metabolic waste from the cerebral parenchyma. Thus, we extend the knowledge of CSF flow and expand the understanding of connectivity between the CNS and peripheral organs.

ependymal cells | F-actin | hepatic stellate cells | cerebrospinal fluid | 5-HT_{2B} receptors

Significance

We show how the cerebrospinal fluid (CSF) can reach peripheral organs through the space surrounding peripheral axons, the periaxonal space. We found that stimulation of 5-HT_{2B}receptors on ependymoglia by either exogenous serotonin or by the optogenetic activation of serotonergic terminals apposing the ependymal layer accelerates the redistribution of CSF from the brain and a spinal cord to peripheral organs. Thus, our study reveals an undescribed mode of communication between the CNS and peripheral organs, representing a pathway for brain-body communication.

The cerebrospinal fluid (CSF) fills up and circulates through the brain's ventricular system, the central canal of the spinal cord, and the subarachnoid space. The CSF is mainly produced by choroid plexi, located in the lateral, third, and fourth ventricles. The average volume of CSF in mice is around 50 µL, while the CSF volume in humans ranges between 150 and 300 mL (1–4). The CSF in humans is produced at a rate of ~500 to 600 mL/day (or ~350 µL/min), thus being fully replaced every ~6 h (5). How the large amount of CSF is drained to keep the stability of intracranial pressure is incompletely understood. Classically, the CSF is known to leave the fourth ventricle at three locations, the foramina of Magendie (median aperture) and Luschka (lateral apertures) to drain into the subarachnoid space. Alternatively, a fraction of the CSF travels along the central canal of the spinal cord. The CSF has many functions (5, 6): it provides a pathway for long-range volume transmission by metabolites and neuroactive substances, including neurotransmitters, peptides, extracellular vesicles, and immunocompetent molecules (7). Neurotransmitters and hormones are secreted to the CSF to mediate long-range signaling (8). Whether the CSF can reach peripheral organs through cranial and peripheral nerves that form the peripheral CSF outflow pathway was not studied in detail earlier. Similarly unknown are the mechanisms regulating CSF efflux from the ventricular system to peripheral organs.

Ependymal glia (or ependymocytes) are a direct scion of radial glia, a class of homeostatic cells of the brain (9). Ependymal glia are connected into a functional syncytium through gap junctions (10, 11); ependymocytes are electrically nonexcitable, relying on intracellular ionic (mainly Ca^{2+}) signaling that propagates throughout their syncytia, and expressing neurotransmitter receptors, with many of them receiving synaptic inputs from neurons (8). Here, we found that the stimulation of ependymocytes of the spinal canal with serotonin (5-HT) triggers the rapid contraction of their actin cytoskeleton. The subsequent volumetric decrease of ependymocytes could open a route for CSF to flow from the nervous system through peripheral nerves toward peripheral organs.

Results

Identification of CSF Flow from the Ventricular System to the Liver. Cadaverine linked to Alexa Fluor 647 (1 kDa) was injected into the cisterna magna (CIM; 5 µL, 20 mg/mL; Fig. 1*A*). The injected dye distributed from the CIM to the brain, spinal cord,

Author contributions: A.V., M.X., and B.L. designed research; X.L., S.W., D.Z., Y.F., Y.L., W.Y., and L.C. performed research; X.L., S.W., D.Z., and T.H. analyzed data; and T.H., A.V., M.X., and B.L. wrote the paper.

The authors declare no competing interest.

This article is a PNAS Direct Submission. M.N. is a guest editor invited by the Editorial Board.

[1]To whom correspondence may be addressed. Email: alexej.verkhratsky@manchester.ac.uk, xiamaosheng1981@163.com, or bmli@cmu.edu.cn.

This article contains supporting information online at https://www.pnas.org/lookup/suppl/doi:10.1073/pnas.2400024121/-/DCSupplemental.

Published November 1, 2024.

nerve branches, and subsequently appeared in liver and pancreas (Fig. 1*B*). Cadaverine propagated from the CIM to cauda equina in 30 min (Fig. 1*B*), and its fluorescence was detected in the liver 4 h after its intra-CIM injection (*SI Appendix*, Fig. S1*A*). After 12 h, the cadaverine disappeared from both the CNS and peripheral organs (Fig. 1*B*). To further characterize CSF flow from CNS to the periphery, FITC-D40 (40 kDa) and TR-D3 (3 kDa) were coinjected into the CIM. Four hours after injection, we monitored FITC-D40 and TR-D3 fluorescence in the brain (anterior section: bregma +0.62 mm and posterior section: −1.34 mm), brainstem (Bregma −6.12 mm), cervical (C3), thoracic (T5), and lumbar (L3) sections of the spinal cord, and the liver and pancreas (Fig. 1 *C*–*E* and *SI Appendix*, Fig. S1 *B*–*D*). In the spinal cord, 4 h after injection, TR-D3 was distributed from central canal into the parenchyma, as shown by the increase in its red-shifted fluorescence signal (*SI Appendix*, Fig. S1*B*). Likewise, FITC-D40, a green fluorescent tracer, was found in both the gray and white matters of the spinal cord parenchyma (*SI Appendix*, Fig. S1*C*). In the liver, 4 h after injection, TR-D3 was seen in hepatic stellate cells (HSCs); which were labeled either with vimentin (Fig. 1*D*) or smooth muscle α-actin (α-SMA, Fig. 1*E*), a cytoskeletal protein (12) broadly used as a marker of HSC activation (13). Similarly, TR-D3 was detected in pancreatic stellate cells that were α-SMA positive (*SI Appendix*, Fig. S1*D*).

To exclude CSF refluxing through the superior vena cava, meningeal lymphatic vessels (14) or anastomoses between CSF and vessels by fenestrations in the perivascular space (15), and also to confirm the primary contribution of spinal nerves as a route of CSF efflux, either the head branch of the superior vena cava was ligated or spinal nerves were sectioned, respectively, and the emergence of TR-D3 in the liver was tested 4 h after its CIM injection (Fig. 2 *A*–*C*). When the head branch of the superior vena cava, which collects the lymph and blood from the brain, was ligated (*SI Appendix*, Fig. S2*A*), the level of TR-D3 fluorescence in the liver decreased to 73.87% ± 5.97% of the control group ($P = 0.012$; $n = 6$; Fig. 2*C*). In contrast, transection of the spinal nerves (T2–T12) that innervate the liver (*SI Appendix*, Fig. S2*B*) decreased the fluorescence intensity of TR-D3 accumulating in the liver parenchyma to 30.93% ± 6.42% of the control group ($P < 0.001$; $n = 6$; Fig. 2*C*). To characterize the flow route(s) of CSF along spinal nerves in detail, Thy1-YFP mice in which the somata and axons are fluorescently labeled were injected with TR-D3 in the CIM. Spinal nerves (T7–T9) were surgically exposed and the ventral spinal nerve was imaged distal to the junction of the posterior and anterior roots with two-photon microscopy. TR-D3 reached the nerve trunks within ~35 to 55 min after CIM infusion, and moved in bulk along the nerve toward the periphery (Fig. 2 *D* and *E* and Movie S1). Thus, we suggest that the CSF can exit the spinal central canal, reside in the spinal cord parenchyma and drain along peripheral spinal nerves.

Next, we addressed the particular compartment(s) supporting CSF flow through (and/or around) the nerves in Thy1-YFP mice, again employing TR-D3. Four hours after intra-CIM injection of TR-D3, the spinal (T7–T9; Fig. 2*F*) and sciatic nerves (Fig. 2*G*)

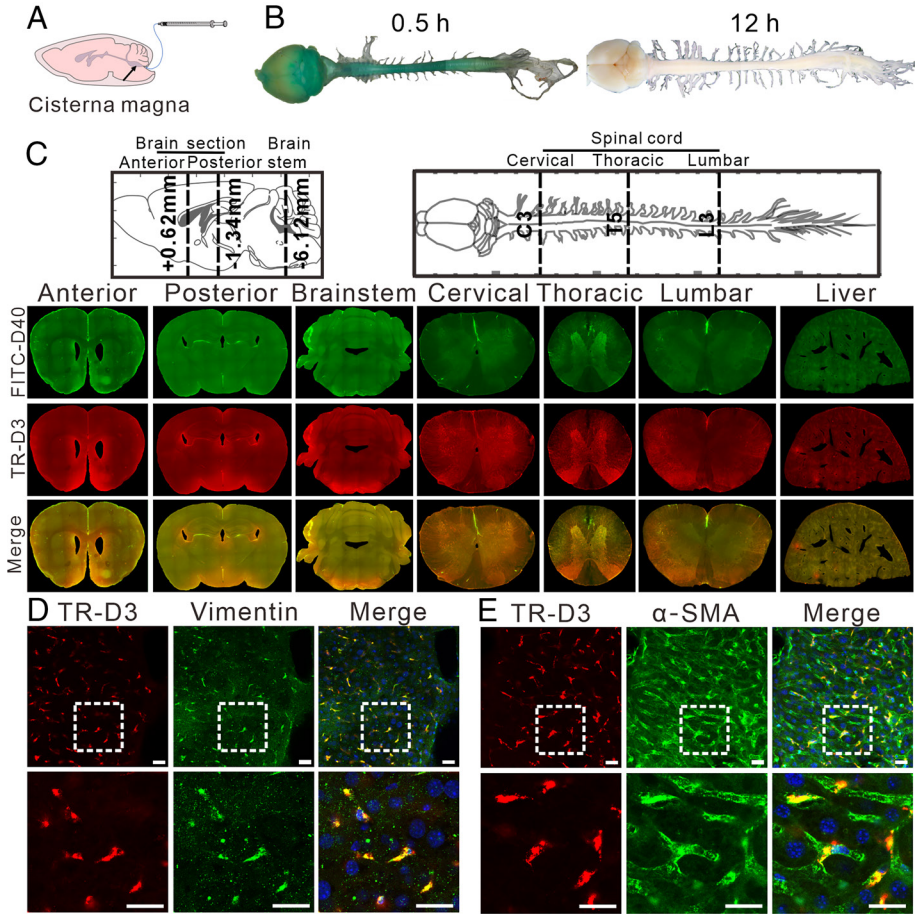

Fig. 1. Delivery of CSF from CIM into the liver. (*A*) The schematic of tracer injection into CIM at 5 μL (20 mg/mL). (*B*) *Left*: images of the brain and spinal cord 30 min after cadaverine CIM-injection. *Right*: same image 12 h after injection. (*C*) Representative images of fluorescent tracers FITC-D40 (green) and TR-D3 (red) in anterior and posterior brain sections, brainstem, cervical, thoracic, and lumbar spinal cord, and in the liver. (*D*) Representative images of TR-D3 fluorescence (red) in liver costained with vimentin (green) and nucleus marker DPAI (blue). (Scale bar, 20 μm.) (*E*) Representative images of fluorescence of TR-D3 (red) in liver costained with α-SMA (green) and nucleus marker DPAI (blue). (Scale bar, 20 μm.)

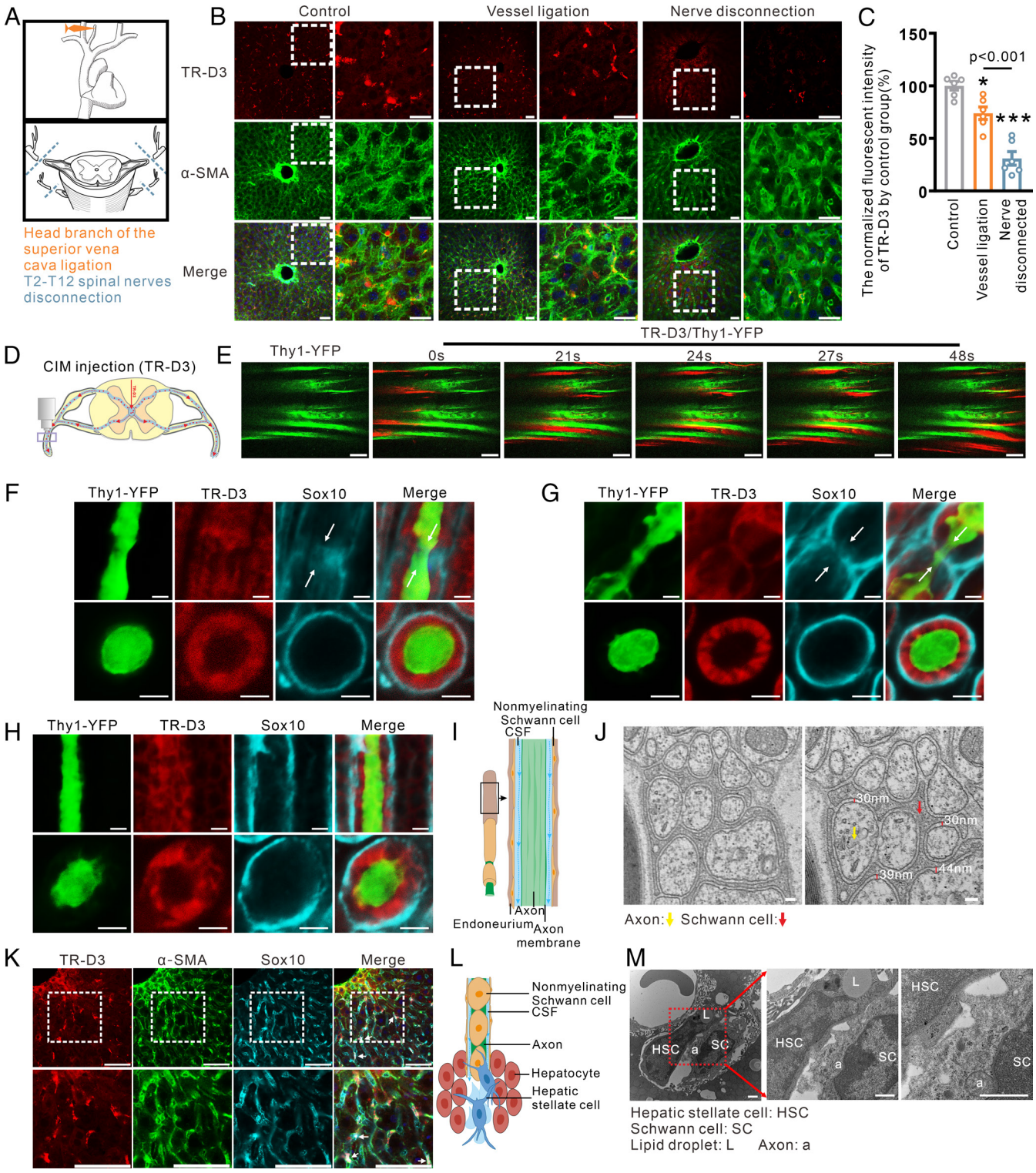

Fig. 2. CSF connects to periaxonal space (PAS) pathway. (*A*) *Upper* panel: the schematic of the head branch of superior vena cava ligation. *Below* panel: the schematic of the spinal T2–T12 nerves disconnection. (*B*) After the operation of superior vena cava ligation or spinal nerves disconnection, TR-D3 was injected into CIM for 4 h, the liver tissues were observed. Representative fluorescence images of TR-D3 (red) distributed in liver costained with α-SMA (green) after ligation of the head branch of superior vena cava or cutting off the spinal nerves T2–T12 segments. (Scale bar, 25 μm.) (*C*) The fluorescent intensity of TR-D3 normalized by control group. Open circles represent data from individual mice (n = 6) and bars represent averages ± SEM; when comparison with control group $^{*}P < 0.05$, $^{***}P < 0.001$. (*D*) Anatomical location of observation window for imaging spinal nerves. (*E*) The images of red TR-D3 distributing along green YFP+ labeled axon of the spinal nerves in Thy1-YFP transgenic mice. (Scale bar, 100 μm.) (*F*) Representative images of longitudinal and cross sections of TR-D3 fluorescence (red) and Sox10 (green) of spinal nerves. (Scale bar, 5 μm.) (*G*) Representative images of longitudinal and cross sections of TR-D3 fluorescence (red) and Sox10 (green) of sciatic nerve. (Scale bar, 5 μm.) (*H*) Representative longitudinal and cross section images of fluorescent tracer TR-D3 (red), Sox10 (cyan), and Thy1-YFP (green) in the nerve roots separated from the hepatic nerve plexus, 4 h after TR-D3 was injected into CIM. (Scale bar, 5 μm.) (*I*) The schematic diagram of CSF flowing in the PAS. (*J*) The representative electron microscope images of axon (yellow arrow) and Schwann cell (SC) (red arrow) in non-myelin axon of the hepatic nerve plexus. The red bar was the measured distance. (Scale bar, 100 nm.) (*K*) The representative images of fluorescent tracer TR-D3 (red) costained with α-SMA (green), Sox10 (cyan), and DAPI (blue) in the liver 4 h after TR-D3 was injected into CIM at. The overlapping images of TR-D3, α-SMA, and Sox10 are indicated by arrows. (Scale bar, 100 μm.) (*L*) The schematic diagram of the proposed connection between SCs and HSCs. (*M*) The representative electron microscope images of HSC, SC, axon (a), and lipid droplet (L) in the liver. (Scale bar, 1 μm.)

were costained for Sox10, a prototypic marker of SCs. TR-D3 fluorescence appeared in close association with YFP$^+$ axons and SCs in both spinal (Fig. 2*F*) and sciatic nerves (Fig. 2*G*), as revealed by volumetric imaging. We interpreted this finding as TR-D3 flowing through the PAS that is delimited by the endoneurium. TR-D3 even delineated the nodes of Ranvier (Fig. 2 *F* and *G*), suggesting that the tracer did not evade the PAS encased by the endoneurium.

The liver is innervated mainly by nonmyelinating axons of sympathetic splanchnic and parasympathetic vagal nerves, as well as by branches of the right phrenic nerves with mixed sympathetic and somatic spinal axons arising from T7 to T12 (16). TR-D3 was in close association with YFP$^+$ axons, as well as Sox10$^+$ SCs (Fig. 2*H*), supporting CSF flow along the PAS (Fig. 2*I*). Ultrastructural analysis of nonmyelinated nerves reinforced the existence of PAS, the size of a gap between the axonal membrane and SCs was ~30 to 40 nm (Fig. 2*J*). In addition, the distribution of TR-D3 being limited to the PAS was evident in spinal (*SI Appendix*, Fig. S2*C*) and sciatic nerves (*SI Appendix*, Fig. S2*D*), and the plexus hepaticus (*SI Appendix*, Fig. S2*E*). Data from wild-type mice (*SI Appendix*, Fig. S2 *F* and *G*) confirmed TR-D3 fluorescence in the spinal and sciatic nerves. In the liver, axons demarcated with Sox10 were proximal to α-SMA$^+$ HSCs (Fig. 2*K*; see *SI Appendix*, Fig. S2*I* for technical controls). We reckon, therefore, that TR-D3 reached the extracellular space, possibly through axonal–stellate cells' junctions (see also, Fig. 2*L*). Ultrastructural data lent further support to the association of HSCs and SCs (Fig. 2*M*).

5-HT Increases T2 Weighted Signal from CSF Compartments in the Spinal Cord. Ventricular ependymocytes receive synaptic contacts and express receptors to various neurotransmitters (17, 18). Ependymocytes are innervated by serotonergic (5-HTergic) efferents from the cerebral region of the raphe complex, and express 5-HT receptors (19, 20). Whether ependymocytes of the central canal receive synaptic inputs was not documented previously. Based on correlated light- and electron microscopy, we show that Thy1-YFP$^+$ axons (of unspecified origin) likely appose α-SMA$^+$ ependymocytes (21) (Fig. 3*A*). Electron microscopy verified that axons and putative synapses surrounded ependymocytes (Fig. 3*B*), even if their neurotransmitter identity remains hitherto unresolved.To test whether 5-HT could modulate the peripheral distribution of CSF, we injected 5-HT at 1.76 µg/mL and 176 ng/mL diluted in ACSF into the CIM of rats and mice, respectively. Considering the dilution of bolus-delivered 5-HT in the CSF, these doses approximate ~100 pmol/mL of 5-HT in CSF, which is within the physiologically effective range (1 to 100 pmol/mL) of this neurotransmitter (22, 23). When acquiring T2-weighted MRI images of the brain and cervical spinal cord segments (Fig. 3*C*), increased signal intensity was reflective of more CSF (Fig. 3 *D* and *E*). Coronal image slabs were collected separately at Bregma –1.30 mm, –4.30 mm, –6.30 mm, –11.30 mm, and –12.3 mm, to calculate within-area signal intensities for the lateral ventricle (LV), dorsal third ventricle (D3V), aqueduct (Aq), and anterior and posterior fourth ventricles (4 V). In spinal cord sections, the calculated signal intensities included the parenchyma, subarachnoid space, and nerve roots, if discernible. The ventricular area within the LV, D3V, and anterior 4 V did not change after 5-HT injection ($P = 0.104$, $P = 0.071$, $P = 0.424$, respectively, $n = 6$; Fig. 3*D*). The area of the Aq and posterior 4 V were, however, significantly reduced by 5-HT ($P < 0.001$ and $P = 0.046$, respectively, $n = 6$; Fig. 3*D*). Injection of 5-HT diminished the CSF content of the LV ($P = 0.014$; $n = 6$), D3V ($P = 0.045$, $n = 6$), Aq ($P < 0.001$, $n = 6$), and posterior 4 V ($P = 0.014$, $n = 6$), but not the anterior 4 V ($P = 0.061$, $n = 6$; Fig. 3 *C–E*). Conversely, 5-HT significantly increased the intensity of MRI signals in cervical spinal cord segments (Fig. 3*E*). At +4.00 mm and +6.00 mm of the cervical spinal cord, the respective signal intensities were increased to 173.63% and 222.35% of the control group ($P = 0.033$, $P = 0.033$; $n = 6$). We also compared the MRI images before and after 5-HT application, as compared with the absence of 5-HT in the same rat. Here, 5-HT decreased the area and T2-weighted signal intensity of the cerebral ventricles, whereas the T2-weighted intensity for the cervical spinal cord was increased (*SI Appendix*, Fig. S3*A*). To further identify the effects of 5-HT on the distribution of CSF, the cerebral region of the dorsal raphe nucleus was injected with adeno-associated virus 2 (AAV2) vectors based on the *Pet-1* promoter to achieve reliable 5-HTergic neuron-specific transgene expression (24) while also delivering hChR2(H134R) for the optical probing of functional coupling (*SI Appendix*, Fig. S3 *B* and *C*). Three weeks after virus delivery, light stimulation of transfected 5-HT neurons significantly increased the peripheral distribution of both TR-D3 and FITC-D40 fluorescence, relative to the control group ($P < 0.001$; $n = 6$; *SI Appendix*, Fig. S3 *D–F*).

The potential expression of 5-HT$_{2B}$Rs in ependymocytes lining the spinal central canal was supported by immunocytochemistry (*SI Appendix*, Figs. S4*A* and S5 *A–F*), which accords the mRNA profile of 5-HT receptor subtypes in primary cultured ependymal cells (25). 5-HT$_{2B}$R-like immunoreactivity was localized to both the luminal and basal surface of ependymocytes, with F-actin concentrating at the luminal surface with some overlap between 5-HT$_{2B}$R-like and F-actin labeling. In the LV, 5-HT$_{2B}$R-like signal was localized to ependymocytes coimmunolabeled with either α-SMA (*SI Appendix*, Fig. S5*G*) or F-actin (*SI Appendix*, Fig. S5*H*).

The Effect of 5-HT on Ependymocytes. Functional consequences of the stimulation of 5-HT receptors were first analyzed in primary cultured ependymocytes labeled with 3 µM calcein (Fig. 4 *A–C*). 5-HT application to the culture medium (100 nM final concentration) gradually decreased the surface area of ependymocytes (Fig. 4*B*): after 10 min of continuous 5-HT exposure, the cellular surface area decreased to 56.69% ± 1.62% of vehicle-treated controls ($P < 0.001$, $n = 12$; Fig. 4*C*). This change was reversible: a single brief application of 5-HT to the cultures triggered transient cell shrinkage, which recovered to their initial surface areas in ~6 min after 5-HT challenge (Fig. 4 *D–F* and Movie S2) (Fig. 4*F*). Pretreatment with methylergometrine maleate (MM), a nonselective 5-HT receptor antagonist, as well as SB204741, a 5-HT$_{2B}$R antagonist, attenuated the morphometric response of ependymocytes to 5-HT. In the presence of SB204741 and 5-HT, the area of ependymocytes was 77.09% ± 2.37% ($P < 0.001$, $n = 12$) of the control values, and SB204741 also prevented, albeit incompletely, the reduction of ependymal area by 5-HT ($P < 0.001$, $n = 12$; Fig. 4*C*). Next, ependymocytes and astrocytes were cocultured in glass cubicles to simulate their multicellular microenvironments in vitro (*SI Appendix*, Fig. S6 *A* and *B*) with 5-HT administration again provoking the contraction of ependymocytes (*SI Appendix*, Fig. S6 *C* and *D*).

Changes in ependymocyte volume are likely mediated by the reorganization of the contractile actin cytoskeleton (26). We confirmed F-actin expression in ependymocytes both in vivo and in vitro by localizing F-actin at the luminal surface of ependymocytes costained for vimentin and α-SMA in vivo (*SI Appendix*, Fig. S6*E*), as well as in culture (*SI Appendix*, Fig. S6*F*). In cultured ependymocytes, F-actin was also visualized by Sir-Actin (Fig. 4*G*). A morphometric change of ependymocytes in response to 5-HT

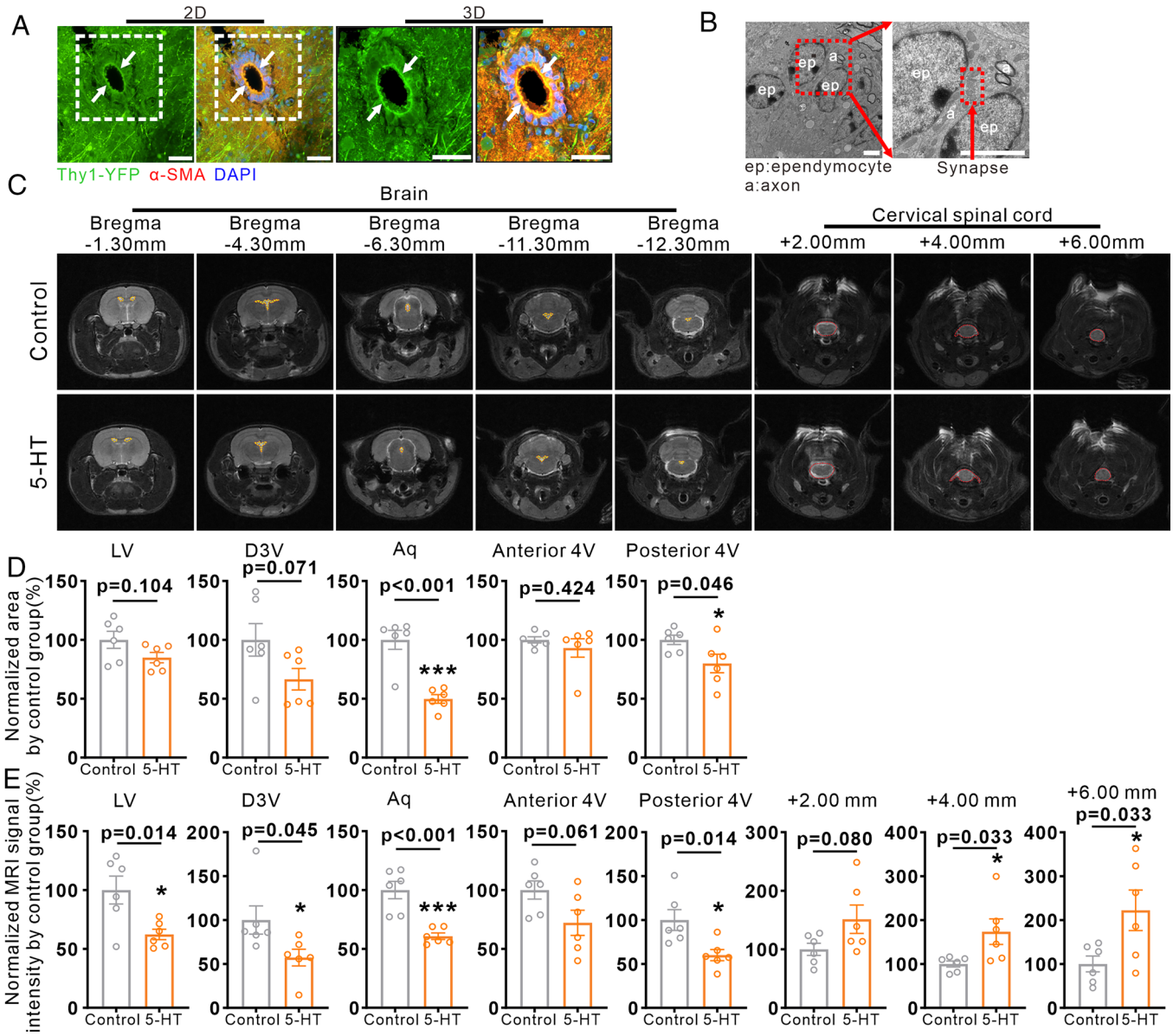

Fig. 3. 5-HT modulates the CSF distribution as revealed by MRI. (*A*) Representative 2D and 3D images of spinal central canal surrounded with green YFP-labeled axons and costained with α-SMA (red) and DAPI (blue) in Thy1-YPF mice. (Scale bar, 50 μm.) (*B*) Representative electron microscope images of ependymocytes (ep), axon (a), and perisynaptic structure delineated by the box. (Scale bar, 2 μm.) (*C*) Representative MRI images of cerebral ventricles and cervical spinal cord in the rats treated with ACSF (control group) and in the rats treated with 5-HT. Yellow dotted lines delineate regions used to estimate the area of cerebral ventricles, and the red dotted lines delineate regions for MRI signal intensity measurements indicating the CSF content. (*D*) The area of cerebral ventricles (labeled by yellow dotted lines) normalized by control group. Open circles represent data from individual rats ($n = 6$) and bars represent mean ± SEM, as comparison with control group $^*P < 0.05$, $^{***}P < 0.001$. (*E*) The MRI signal intensities of cerebral ventricles and cervical spinal cord (labeled by red dotted lines) normalized by control group. Open circles represent data from individual rats ($n = 6$) and bars represent mean ± SEM, as comparison with control group $^*P < 0.05$, $^{***}P < 0.001$.

was associated with the redistribution of F-actin, as shown by its increased fluorescence intensity when the cellular surface became reduced (Fig. 4*H*). Exposure of primary ependymocytes to 5-HT significantly increased $[Ca^{2+}]_i$ (Fig. 4 *I* and *J* and Movie S3), to 157.90% ± 2.78% of the baseline ($P < 0.001$; $n = 12$; Fig. 4*K*). Pretreatment with either SB204741 or the Ca^{2+} chelator BAPTA-AM suppressed 5-HT-induced $[Ca^{2+}]_i$ rise ($P < 0.001$, $P < 0.001$, respectively, $n = 12$; Fig. 4 *I*–*K*). When monitoring $[Ca^{2+}]_i$ together with F-actin, we found that a 5-HT-induced increase in $[Ca^{2+}]_i$ correlated with the aggregation of F-actin (Fig. 4 *L* and *M*). BAPTA-AM prevented the shrinkage of ependymocytes in response to 5-HT (*SI Appendix*, Fig. S6*G* and Fig. 4*N*). These data suggest that ependymocytes respond to 5-HT by cytoskeletal reorganization that could affect their size and coupling, even in vivo.

5-HT Affects Distribution of CSF Tracer with a Shift Toward Spinal Cord. Intra-CIM administration of 5-HT together with TR-D3 significantly increased TR-D3 fluorescence in HSCs after 4 h CIM-injection ($P < 0.001$, $n = 6$). Pretreatment with SB204741 ($P < 0.001$, $n = 6$) or BAPTA-AM ($P < 0.001$, $n = 6$) partly negated this effect of 5-HT (Fig. 5 *A*–*C*). To further characterize CSF movement from the ventricular system toward the liver, trisodium citrate ($C_6H_5Na_3O_7$; MW = 258.07) was injected into the CIM (70 mM diluted in 5 μL ACSF; 18 mg/mL). After 4 h, the brain, brainstem, thoracic spinal cord, hepatic plexus, and liver were dissected out, and the level of trisodium citrate was measured by liquid chromatography–mass spectrometry (LC–MS; *SI Appendix*, Fig. S7 *A*–*D*). As compared with control levels from the same tissues (Fig. 5*D*), 5-HT significantly decreased the trisodium citrate content by 28.82% ± 3.64% in the brain ($P < 0.001$, $n = 6$), and by 39.15% ± 4.91% in

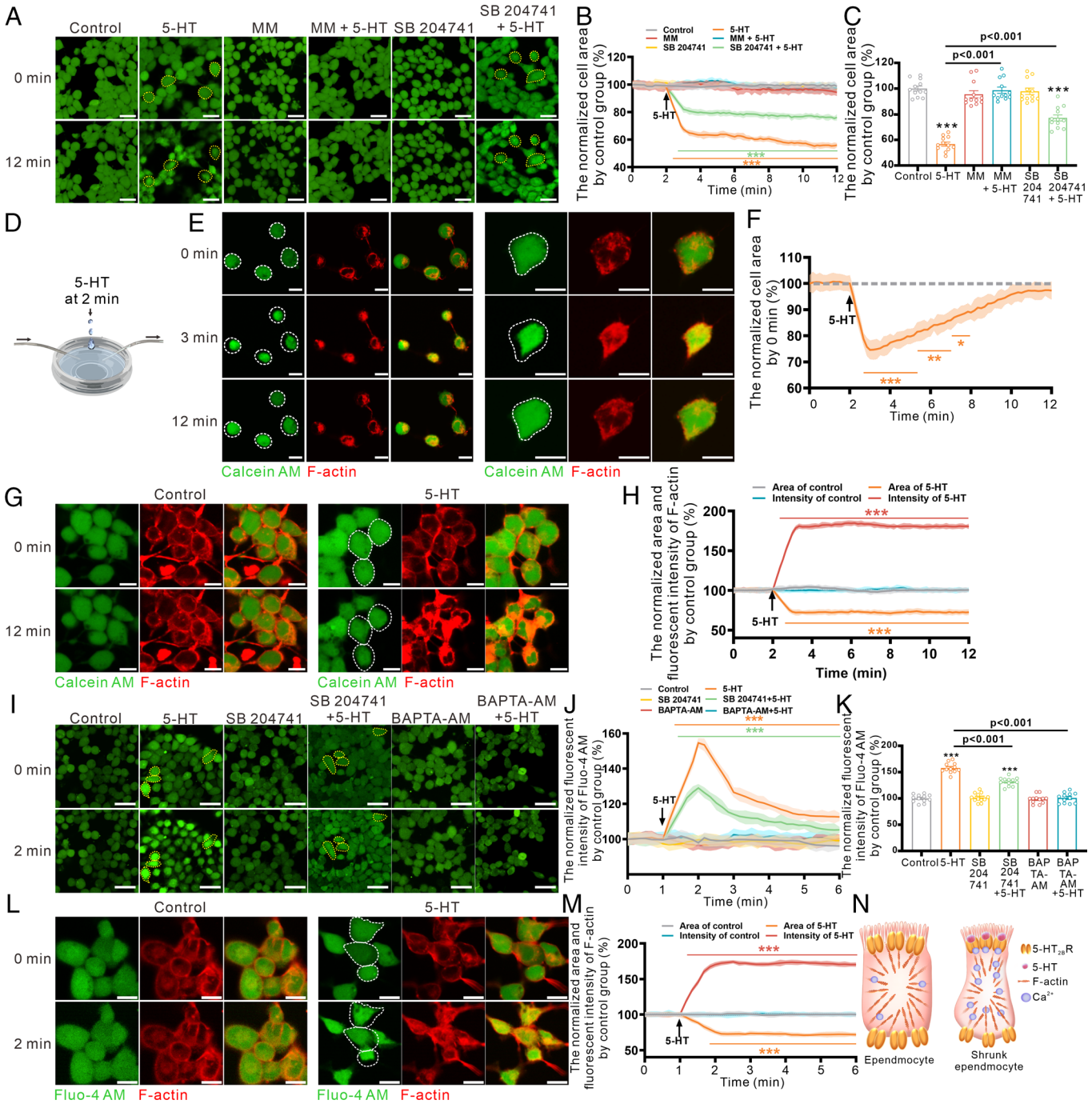

Fig. 4. The 5-HT-induced ependymal shrinkage is mediated by 5-HT_{2B}R and consequent cytoplasmic Ca^{2+} increase induced F-actin polymerization. (*A*) Representative image of calcein-AM labeled ependymocytes at 0 and 12 min of time lapse recording. Primary cultured cells were exposed (for 10 min) to 5-HT alone or after 15 min pretreatment with MM (broad antagonist of 5-HT receptors) or SB204741 (selective antagonist of 5-HT_{2B}R), then exposed to isotonic solution (control) or 5-HT for 10 min. (Scale bar, 25 μm.) (*B*) Changes of cellular area in response to 5-HT alone or in the presence of 5-HT receptors antagonists as indicated on the graph. Cell area was normalized to control group, every line shows mean values; while shadow shows SEM for every time point (acquired every 10 s); $n = 12$ experiments. ***$P < 0.001$. (*C*) The percentage of calcein-AM fluorescence intensity normalized by control group at 12 min. Open circles represent data from individual cultured batch ($n = 12$) and bars represent averages ± SEM, as comparison with control group ***$P < 0.001$. (*D*) Schematic of the added 5-HT into the flowing culture medium at 2 min. (*E*) Representative images of calcein-AM labeled ependymocytes at 0, 3, and 12 min of time lapse recording. Primary cultured cells were exposed to brief application of 5-HT at 2 min while the culture medium was constantly flowing. (Scale bar, 10 μm.) (*F*) Changes of cellular area in response to 5-HT. Cell area was normalized to control group, every line shows mean values; while shadow shows SEM for every time point (acquired every 10 s); $n = 12$ experiments. **$P < 0.01$, ***$P < 0.001$. (*G*) Representative images of the calcein-AM and F-actin labeled ependymocytes. Primary cultured ependymocytes were labeled by calcein-AM and Sir-actin (F-actin), then incubated with 5-HT for 10 min. (Scale bar, 10 μm.) (*H*) Area and fluorescent intensity of F-actin normalized by control group at twelfth minute. Solid lines represent the mean for separate cultures ($n = 12$); shaded areas indicate SEM as compared to the control group ***$P < 0.001$. (*I*) Representative image of Fluo4-AM labeled ependymocytes in them presence of 5-HT alone or after 15 min pretreatment with SB204741 or BAPTA-AM at 0 and 2 min of recording (peak of $[Ca^{2+}]_i$ increase). (Scale bar, 25 μm.) (*J*) Intracellular Ca^{2+} dynamics (expressed as Fluo-4 intensities normalized to control). Lines represent the mean ± SEM for every time point (acquired every 10 s); $n = 12$ experiments. ***$P < 0.001$. (*K*) Fluo-4 fluorescent intensity normalized to control group at 2 min. Open circles represent means from individual ($n = 12$) and bars represent averages ± SEM, as compared to control group ***$P < 0.001$. (*L*) Representative images of the Fluo-4-AM and F-actin labeled ependymocytes incubated with 5-HT for 5 min. (Scale bar, 10 μm.) (*M*) Area and fluorescent intensity of F-actin normalized to control group at 6 min. Solid lines represent the means of individual experiments ($n = 12$) and shaded areas indicate SEM, as compared to control group ***$P < 0.001$. (*N*) Schematic of the shrunk ependymocytes following polymerization of F-actin triggered by the 5-HT-induced $[Ca^{2+}]_i$ increase.

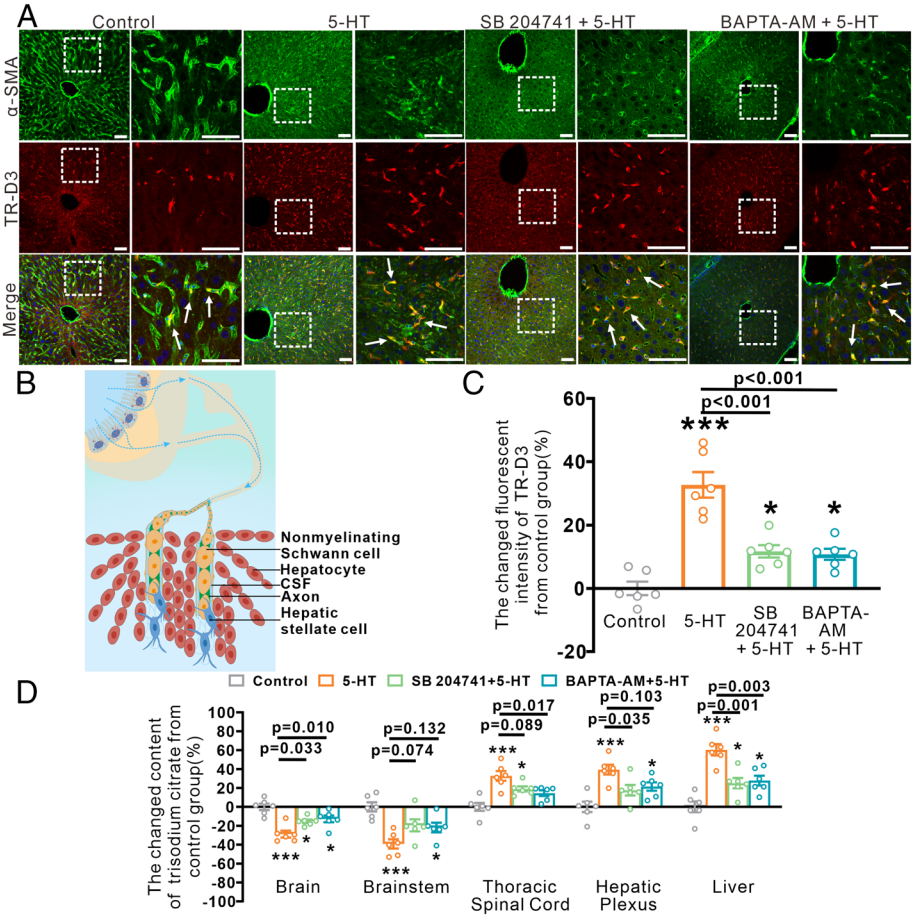

Fig. 5. Delivery of fluorescent markers form the CNS into the liver is 5-HT_{2B}R and Ca^{2+} dependent. (*A*) Representative images of TR-D3 fluorescence costained with α-SMA (green) and DAPI (blue) in the liver. (Scale bar, 100 μm.) (*B*) Schematic depiction of CSF flow through PAS into the liver. (*C*) Fluorescence intensities of TR-D3 normalized to control; open circles represent data from individual mice ($n = 6$) and bars represent mean ± SEM, $^*P < 0.05$, $^{**}P < 0.01$. (*D*) Trisodium citrate levels measured by HPLC-MS 4 h after CIM injection in the brain, brainstem, thoracic spinal cord, hepatic plexus, and liver. Open circles represent data from individual mice ($n = 6$) and bars represent averages ± SEM, as comparison with control group $^*P < 0.05$, $^{**}P < 0.01$, $^{***}P < 0.001$.

the brainstem ($P < 0.001$, $n = 6$). In contrast, trisodium citrate levels were increased by 32.72% ± 5.14% in the thoracic spinal cord ($P < 0.001$, $n = 6$), by 39.36% ± 5.19% in the hepatic plexus ($P < 0.001$, $n = 6$), and by 60.35% ± 5.97% in the liver ($P < 0.001$, $n = 6$). Pretreatment with both SB204741 and BAPTA-AM occluded the 5-HT effects.

Thereafter, we measured both TR-D3 and FITC-D40 fluorescence in acutely isolated brain slices from the forebrain, brainstem, cervical, thoracic, and lumbar spinal cord segments and in the liver 4 h after CIM injection (*SI Appendix*, Figs. S8 and S9). Exposure to 5-HT reduced FITC-D40 intensity in the anterior and posterior brain by 61.62% ± 1.39% ($P < 0.001$, $n = 6$) and 50.77% ± 1.23% ($P < 0.001$, $n = 6$) of the control, respectively. In contrast, TR-D3 fluorescence was reduced by 56.92% ± 3.19% ($P < 0.001$, $n = 6$) and 56.93% ± 5.56% ($P < 0.001$, $n = 6$) in the respective areas. In the brainstem, the intensities of FITC-D40 and TR-D3 decreased by 61.78% ± 1.71% ($P < 0.001$, $n = 6$) and 54.36% ± 2.91% ($P < 0.001$, $n = 6$) of the control group, respectively. In the cervical spinal cord, the intensities of FITC-D40 and TR-D3 were increased to 168.26% ± 3.16% ($P < 0.001$, $n = 6$) and 156.30% ± 3.93% ($P < 0.001$, $n = 6$) of the control group, respectively. A similar tendency was observed in slices from thoracic and lumbar spinal cord. Intensities of FITC-D40 were elevated by 40.88% ± 3.61% ($P < 0.001$, $n = 6$) and 96.37% ± 3.72% ($P < 0.001$, $n = 6$) of the control group, while the intensities of TR-D3 were increased by 70.20% ± 2.70% ($P < 0.001$, $n = 6$) and 71.12% ± 4.27% ($P < 0.001$, $n = 6$) of the controls. Pretreatment with MM, SB204741, and BAPTA-AM antagonized the effects of 5-HT on FITC-D40 and TR-D3 propagation from the CNS to the liver (*SI Appendix*, Figs. S8*C* and S9*B*). We attributed these effects to ependymocytes shrinkage; however, it must be stressed that 5-HT can also act on neurons and vasculature which also may affect CSF flow.

Both Noradrenaline and Dopamine Increase CSF Delivery to the Liver. 5-HT was not the only neurotransmitter affecting CSF movement from the nervous system to peripheral organs. Spinal cord ependymocytes potentially express other catecholamine receptors, alike their counterparts that line the third ventricle (e.g., adrenoceptors and dopamine receptors) (27). Norepinephrine (NE) and dopamine (DA) both increased the delivery of fluorescent tracers (FITC-D40 and TR-D3) to the spinal cord and liver, while gradually dissipating from the brain and brainstem (*SI Appendix*, Figs. S8*C* and S9*B*). Inhibition of adrenoceptors by phentolamine mesylate prevented the NE-induced increase in the translocation of fluorescent tracers. Likewise, haloperidol, an inhibitor of dopamine receptors, antagonized DA-induced accumulation of fluorescent tracers in the liver (*SI Appendix*, Figs. S8*C* and S9*B*).

Discussion

Here, we revealed a conduit that links the brain's ventricular system and peripheral organs, and allows for long-range volumetric signaling between the CNS and peripheral organs. We found that tracers with low (cadaverine, 1 kDa), medium (TD-3R, 3 kDa), and high

molecular weight (FITC-D40, 40 kDa) injected into the CIM traveled first to the spinal cord, reached the parenchyma, and then through the PAS of peripheral nerves were delivered to the liver and pancreas. How could the CSF enter the spinal cord parenchyma and hence the PAS? Conceptually, the CSF could flow though the subarachnoid space entering the spinal glymphatic system or through the central canal. The latter, while lesser in volume, also involves crossing the ependymal wall. We addressed the possible role of ependymoglia in the regulation of CSF movement from the central canal to the spinal cord parenchyma. We hypothesize that ependymal cells act as a physical barrier controlling CSF entry to the spinal cord. As yet, we cannot exclude the role for subarachnoid and/or glymphatic flow. Moreover, the relative contribution of different pathways may change with age, as in humans, for example, the spinal canal obliterates in an age-dependent manner (28). Thus, future experiments need to determine the relative contribution of each CSF pathway to PAS-dependent efflux.

Ependymal Hypothesis. We propose that CSF-to-parenchyma transition, at least in part, is regulated by ependymoglia lining the central canal of the spinal cord. We argue that spinal ependymocytes can regulate CSF movement by the reorganization of their cytoskeleton, thus allowing for changes of cell size, allowing CSF flow toward the PAS. This hypothesis advances existing knowledge on CSF movement, and shows that neurotransmitter-induced changes in the volume of ependymal cells can contribute to the unidirectional flow of CSF.

Cathecholamines Regulate Ependymocytes. Ependymal glia form the wall of both the ventricular system of the brain and the central canal of the spinal cord, erecting a partial barrier between CSF and nervous system parenchyma (9, 29). This barrier, however, does not strictly restrict paracellular water and solute movements, as ependimal cells are not connected by tight junctions. Ventricular ependymocytes receive synaptic catecholaminergic innervation from brainstem nuclei (18, 20). Here, we presented high-resolution neuroanatomy data suggesting the likely synaptic innervation of ependymocytes of the central spinal canal. Functional catecholamine (5-HT, DA, NE) receptor expression (that is, 5-HT_{2B}R for 5-HT) indeed characterized ependymal cells of the spinal cord. Volumetric changes in ependymocytes regulated by catecholamines were mediated by the Ca^{2+}-dependent reorganization of the actin cytoskeleton. The catecholamine-evoked shrinkage of ependymocytes decreased CSF in the cerebrum while increased CSF first within the central canal, then in the parenchyma of the spinal cord, and ultimately in the liver. In the hepatic interstitium, connections between SCs and HSCs facilitated CSF drainage into the liver parenchyma (Fig. 6). Thus, an exquisitely positioned cellular barrier that can undergo rapid remodeling could exist along the spinal cord.

Ependymocytes belong to astroglia, and hence possess classical intracellular excitability, mainly mediated by Ca^{2+} signaling (30). Such excitability is triggered by neurochemical stimulation. Ependymal Ca^{2+} signals were earlier characterized in response to, e.g., 2 mM glucose (31), as well as by the activation of $P2X_7$ purinoceptors (32, 33). Here, we provide evidence that stimulation of metabotropic $5HT_{2B}$Rs also triggers Ca^{2+} signaling in ependymal cells. Ca^{2+} signals set in motion F-actin reorganization, resulting in volumetric changes. It is conceivable to speculate that, under physiological conditions, monoamines regulate the rhythmic (diurnal) fluctuations of CSF flow mediated by dynamic changes in the volumes of ependymal cells. It is also likely that ependymocytes at different segments of the brain's ventricles and

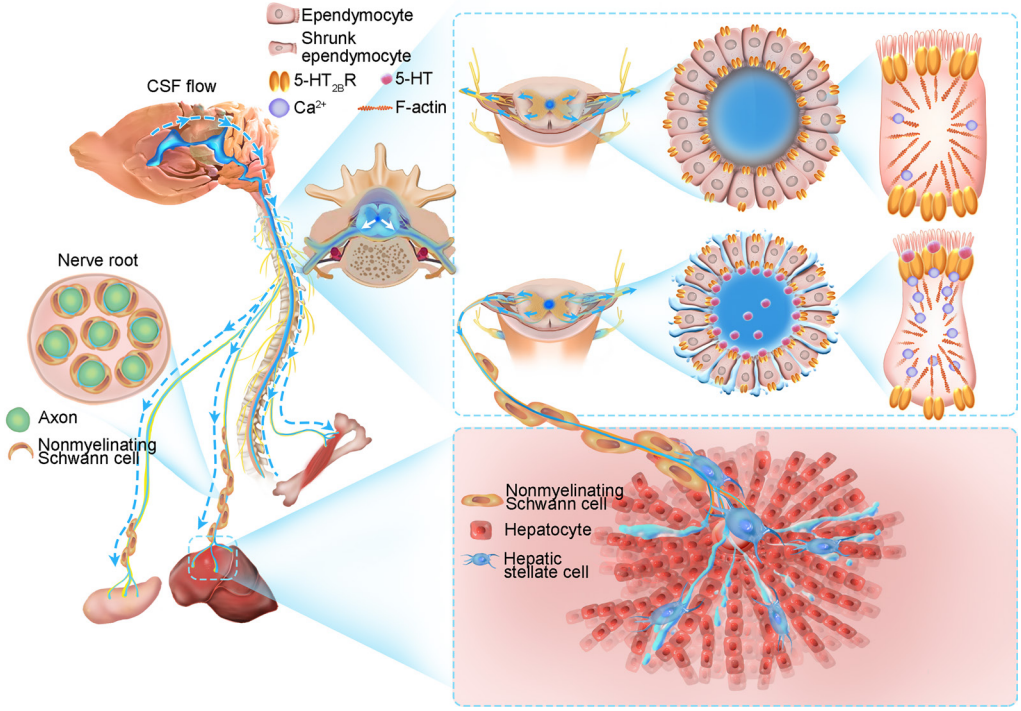

Fig. 6. The schematic of ependymocytes controlling CSF flow from the central canal into peripheral organs along PAS route. In this study, CSF is shown to flow along the PAS pathway from the central canal to peripheral organs, such as the liver, pancreas, and muscles. In this PAS route, CSF mainly flows between the peripheral axons and myelinating and nonmyelinating SCs (the *Left* side). Dynamic volume changes of ependymocytes regulate CSF flow from the CNS into the periphery. The catecholamine neurotransmitter, serotonin, induces ependymocytes shrinkage by acting through 5-HT_{2B} receptors and triggering the intracellular Ca^{2+} signal-dependent polymerization of cytoskeletal protein, F-actin. Serotonin-induced decrease in ependymocytes volume opens one-way gate to facilitate CSF outflow from the central canal into the spinal cord parenchyma and peripheral nerves (*Upper Right* side). Then, CSF moves through PAS along the peripheral nerves until reaching the periphery. In this study, we mainly studied the liver. CSF can flow along the nonmyelinating axons of hepatic plexus nerves and reach liver, wherein CSF could be received by stellate cells (*Lower Right* side). The identified PAS route controlled by ependymocytes represents the novel CSF communicational conduit between the CNS and the periphery.

spinal central canal have distinct sensitivity to neurotransmitters, thus increasing flexibility and precision in the regulation of CSF flow.

In the central canal, ependymocytes possess high levels of F-actin, which could mechanistically contribute to the regulation of the shape and volume of these cells (34, 35). In addition, the F-actin network coordinates cilial movement at the apical surface of the cells (36). Cytosolic Ca^{2+} signals regulate F-actin polymerization and stability (37): in particular, Ca^{2+} binds to F-actin to form Ca^{2+}-F-actin (38). Polymerization of F-actin in *Vibrio splendidus* agglutinated by a subunit of oligomerization domain-like receptors (NLRs) is Ca^{2+}-dependent (39). Similarly, cytoplasmic Ca^{2+} regulates the reorganization of F-actin (40). We propose that stimulation of 5-HT_{2B}Rs triggers Ca^{2+} signals that interact with the actin cytoskeleton to dynamically control the shape and volume of ependymocytes. The subsequent shrinkage of ependymocytes opens up an intercellular conduit for CSF eflow into the spinal parenchyma and toward peripheral nerves. Ependymocytes thus work as "water-gates", whose function can be tuned by synaptic input.

CSF Flow through a PAS. It is established that the CSF clears metabolic waste produced by the brain parenchyma, while its flow is rhythmically fluctuating diurnally (41). It is also known that ependymal cilia beat rhythmically to facilitate unidirectional CSF flow. Although some studies reported that CIM-injected India ink or colored silastic material could be observed in peripheral nerves over time (42, 43), the exact flow pathway was not characterized in detail. Likewise, collection routes of CSF outflow were mainly considered to be associated with the lymphatic system. Thus, CSF outflow along peripheral spinal nerves was hypothesized (44, 45), without the physical nature of the conduit toward peripheral organs being identified.

Our findings support the existence of lymphatic collection routes of CSF (46–48), and the clearance of cerebral parenchymal metabolic waste through the glymphatic system (41, 49, 50). The CSF flows through the PAS pathway, which is delineated by myelinating or nonmyelinating SCs, endoneurium, perineurium, and epineurium (from inside to outside). The subarachnoid space is also filled with CSF arriving mainly from the fourth ventricle (51). The anatomical structure of subarachnoid cul-de-sac, the intact spinal arachnoid, and dura mater arguably restricts CSF outflow along the lateral epineurium of spinal nerves (*SI Appendix*, Fig. S10). Thus, the CSF flowing is continuous in the CNS, and the CSF in subarachnoid space can directly circulate into the spinal central canal from the median aperture (foramen of Magendie) of the fourth ventricle (51).

Conclusions and Future Perspectives. We found that CSF is transported to peripheral organs through the PAS of the spinal nerves. CSF flow may be instrumental for the delivery of many signaling molecules and metabolites, thus adding an unexpected level of complexity to the CNS-dependent control of visceral functions. In this paradigm, it is speculated that the CSF could act as a signaling medium extending from the brain to the peripheral organs. Future investigations of this system, its pathways, cellular constituents, and their regulation could be fundamental for the physiology of CNS-periphery communication in health and disease.

Materials and Methods

Materials. Please see *SI Appendix*, Table S1 for the materials used in this study.

Animals. The male wild-type C57BL/6J mice (#000664) and B6.Cg-Tg(Thy1-YFP) HJrs/J (#003782) transgenic mice were purchased from the Jackson Laboratory (Bar Harbor, ME). Male Sprague–Dawley rats (#22001A, purchased from Hfkbio, Beijing, China) were used for MRI experiments. 10- to 16-wk-old mice and rats were kept in standard rooms at 22 ± 1 °C, maintained on a 12/12 h light/dark cycle, and were given adequate food and water. All experiments were performed under the guidance of the US NIH Guide for the Care and Use of Laboratory Animals (NIH Publication No. 8023) and its 1978 revision. All experimental protocols were approved by the Institutional Animal Care and Use Committee of China Medical University, approval No. [2020]102. Randomization for all animal experiments was performed using a random number table.

Tracers Injection and Detection. We monitored distribution of fluorescent tracers between different parts of the CNS and peripheral organs to trail CSF movements (52–54). The fluorescent tracers TR-D3 and FITC-D40 were dissolved in artificial CSF (ACSF) at 1% (w/v). The male adult mice were fasted before surgery, and anesthetized using ketamine (100 mg/kg) and xylazine (10 mg/kg). Head stereotaxic system was used to fix the mouse while surgically exposing the posterior atlanto-occipital membrane. The tracers were delivered to CSF through CIM injection using a 30 G needle, at a rate of 1 μL/min for 5 min (5 μL total volume). In 4 h after tracer injection, anesthetized mice were fixed by transcardial perfusion with phosphate buffer saline (PBS) and 4% paraformaldehyde (PFA). Tissues were cut into 50 mm slices, images captured using Carl Zeiss Axio Scan microscope (Promenade 10, Jena, Germany) or confocal scanning microscope (DMi8, Leica, Wetzlar, Germany).

ImageJ software (ImageJ 1.46r, NIH) was used to quantify and analyze fluorescence images. Intensities of FITC-D40 and TR-D3 from different groups were normalized to the intensity of the control group. For images scanned with Carl Zeiss AxioScan microscope, we used ImageJ to select regions of interests to calculate mean fluorescence intensity of FITC-D40 and TR-D3; ImageJ was also used to remove background color and quantify the mean fluorescence intensity of TR-D3.

Immunofluorescence Assay and Calculation. As described previously (52), the anesthetized male adult mice were perfused through the heart with PBS and 4% PFA, soaked in 4% PFA and kept for 24 h. After collection, the tissues were cut into uniform slices with a thickness of 60 μm. Tissue slices were incubated with donkey serum for 1 h for permeabilization. Primary antibodies were incubated at 4 °C overnight, followed by secondary antibody incubated at room temperature for 2 h. The staining of F-actin is tissue slices incubation with 100 nM TRITC-phalloidin (YEASEN Biotechnology, Shanghai, China) for 30 min at room temperature after secondary antibodies incubation. Nuclei of cells were marked with its common immunofluorescence marker, DAPI at 1:1,000 dilution. Images were captured using a confocal scanning microscope (DMi8, Leica, Wetzlar, Germany). The specific information on the antibodies used is shown in *SI Appendix*, Table S1.

Ligation of Vena Cava and Sectioning of the Spinal Nerves. Adult male mice were anesthetized with ketamine (100 mg/kg) and xylazine (10 mg/kg). To ligate the head branch of the superior vena cava, the chest cavity was carefully opened to expose the heart, and then the head branch of the superior vena cava was ligated. To disconnect the spinal nerves, the mice were anesthetized as above, bilateral erector spinal muscles were separated to expose the spinal nerves from T2 to T12 on both sides; the nerves were then cut. After the surgical operations, the mice were quickly sutured and kept body temperature around 37 °C until the full awakening.

Tissue Sampling. The anesthetized mice were perfused and fixed with PBS and 4% PFA through the heart. After 15 min, the mouse brain, brainstem, spinal cord, liver, pancreas, cervical lymph nodes, spinal nerve roots, and sciatic nerve were taken for subsequent immunofluorescence experiments. The spinal nerve root is taken from the cervical segment of the spinal cord, located after the intersection of the anterior and posterior roots (near the intervertebral foramen).

Two-Photon Microscopy. The male B6.Cg-Tg(Thy1-YFP)HJrs/J transgenic mice were anesthetized with ketamine (100 mg/kg, i.p.) and xylazine (10 mg/kg, i.p.), mice body temperature was kept around 37 °C. The spinal nerves at the thoracic level from T7 to T9 were exposed, and the observation window of the exposed spinal nerves was perfused with ACSF and observed under the objective. The images of the nerve were taken every 3 s using FluoView with two-photon laser-scanning setup (Nikon A1R, Japan). Bandpass filters (Chroma) were 540 nm/40 nm for YFP and 850 nm/70 nm for TR-D3 signals. The confocal images of the nerve were

taken every 3 s. The red tracer TR-D3 was injected into CIM at a rate of 1 μL/min for 5 min (5 μL total volume). In 35 to 55 min after injection the tracer appeared in the spinal nerves, the observations were started after the injection of TR-D3, the first presence of tracer TR-D3 under observation view was set as 0 s.

Electron Microscopy. In order to fix the liver, spine, and sciatic nerve of mice, PBS, and 2.5% glutaraldehyde were combined. Dissected samples of the liver, spine, and sciatic nerve were cut into 1 mm^3 pieces and fixed at 4 °C in 2.5% glutaraldehyde. After being fixed in a solution consisting of 1% osmium for 2 h at 4 °C, the pieces were rinsed multiple times in PBS, dried on a graduated series of ethanol concentrations ranging from 20% to 100%, then using 100% acetone, penetrated by Epon 812, and then polymers on pure Epon 812 for 72 h at 65 °C. The samples were set up in comparatively thin portions. Using an ultramicrotome, extremely thin slices (70 nm) were cut, gathered in copper grids, and painted using lead citrate and uranyl acetate. The samples in every component underwent TEM (JEM-1400Flash, Japan) examination in 10 visible areas.

MRI Analysis. Rats were anesthetized with 3% and 2% isoflurane. Head stereotaxic instrument was used to fix rats while surgically exposing the posterior atlantooccipital membrane. The ACSF (Control group) or serotonin (5-HT group) was delivered into the CSF of rat through CIM injection at a rate of 1 μL/min for 5 min using a 30 G needle. The injected rats were sutured and then placed in the MRI animal imaging system (Bruker biospec3T, Bruker, Billerica, MA), T2-weighted images were scanned and image acquisition was performed using ParaVision software (ParaVision PV-360.2.0.p1.1, Bruker, Billerica, MA). The scan parameters for the T2-weighted images sequence were axial scan direction, repetition time = 4,538 ms, effective TE = 85 ms, echo time = 15 ms, flip angle = 90°, number of averages = 8, field of view = 35 × 35 mm^2, matrix size = 256 × 256, slice thickness = 1 mm, number of slices = 25. ImageJ (ImageJ 1.46r, NIH) was used to delineate and calculate the areas and MRI signal intensities of the LV, aqueduct, and fourth ventricle, as well as the MRI signal intensities of the high signal area at the cervical spinal cord. The calculated ventricle area of the selected optical planes (yellow dotted lines) was normalized by the total area of the brain tissue in the same optical planes, in order to exclude the individual difference. The liquid content of the selected tissues in the optical planes (red dotted lines) was reflected by MRI signal intensity. At last, the measured data in every group were all normalized to the control group.

Ependymal Cells Culture. Primary cultured ependymal cells were prepared as described previously (55). The newborn mouse brains were aseptically isolated, the tissue was vortexed, filtered, and suspended in MEM_C (MEM containing 5 mg/L insulin, 0.5 g/L BSA, and 10 mg/L transferrin), the suspensions were planted in fibronectin-treated cell culture dishes. After 48 h of static culture, changed the culture medium to MEMcT (MEMc with 500 U/L thrombin). The medium was refreshed completely every three days.

Coculture of Ependymocytes with Astrocytes in Glass Cubicles. Newborn mice within 3 d of birth were used to extract astrocytes as reported previously (54, 56). The neopallia of cerebral hemispheres were isolated and made into single-cell suspensions under sterile conditions. Isolated astrocytes were cultured in a moist environment of carbon dioxide/air at 37 °C, using Dulbecco Minimum Essential Medium (DMEM), with 15% fetal bovine serum as culture medium.

As described previously (57), the cells were harvested (using 0.125% trypsin) and seeded in fibronectin-coated 24-well Transwell® chamber insert (57). The upper chambers were seeded with ependymal cells, and the lower chambers were seeded with astrocytes. Follow-up experiments were carried out when the degree of cell confluence reached about 80%.

Cell Volume Assay. For cell volume monitoring and imaging in cultured ependymocytes, cells were treated with 3 μM calcein AM (Beyotime, Shanghai, China) for 15 min. After PBS containing calcein AM was replaced with PBS without calcein AM, cells were incubated for 10 min, and then tests were carried out. The cell volume of cultured ependymocytes was visualized by calcein signals at 10-s intervals for 12 min using a confocal scanning microscope (DMi8, Leica, Wetzlar, Germany). The cell volume from all calcein positive cells in a field of recording selected for every culture dish used in experiment were included in the statistics, and the cell volume of ependymocytes was normalized to the baseline volume at 0 min. The test was repeated in 12 different cultures using the same method. ImageJ software (ImageJ 1.46r, NIH) was used to quantify the volume.

Cellular Recovery Detection. Cultured ependymocytes were treated with 1 μM Sir-Actin (Cytoskeleton, Denver, CO) for 30 min. After PBS containing Sir-Actin was replaced with PBS without Sir-Actin, cells were incubated with calcein AM as above. Images of cultured ependymocytes cotreated with calcein AM and Sir-Actin were captured at 10-s intervals for 12 min using a confocal scanning microscope (DMi8, Leica, Wetzlar, Germany). During the imaging, two identical constant-flow pumps (BT100-1 J, Longer, Hebei, China) were used to input and output the culture medium at 40 rpm (~100 μL/min) to keep it flowing and to maintain complete equilibrium of the liquid level. 5-HT was added directly to the dish to reach the final concentration ~100 nM. The cell volume from all calcein positive cells in a field of recording selected of every culture dish used in experiment were included in the statistics, the cell volume of ependymocytes was normalized to the baseline volume in 0 min. The test was repeated in 12 different cultures using the same method. ImageJ software (ImageJ 1.46r, NIH) was used to quantify the volume.

Ca^{2+} Imaging and Quantification. As described previously (58), cultured ependymocytes were incubated with 3 μM fluo-4 AM (Beyotime, Shanghai, China) for 15 min. Subsequently PBS containing Fluo-4 was replaced with PBS without Fluo-4, in which cells were incubated for 10 min. The fluorescence signals of Fluo-4 were monitored at 10-s intervals for 6 min by a confocal scanning microscope (DMi8, Leica, Wetzlar, Germany). As previously described (46), all cells labeled with Fluo-4 in a field of recording were included in the statistics. Fluo-4 intensity was normalized to the baseline intensity at the beginning of experiment. The ImageJ software (ImageJ 1.46r, NIH) was used to analyze Ca^{2+} signals. The measurements were repeated in 12 different cultures.

F-actin Assay. To monitor and image F-actin in ependymocytes, cells were treated with 1 μM Sir-Actin (Cytoskeleton, Denver, CO) for 30 min. After PBS containing Sir-Actin was replaced with PBS without Sir-Actin, cells were incubated with calcein AM or fluo-4 AM as above. Images of cultured ependymocytes cotreated with Sir-Actin and calcein AM were captured at 10-s intervals for 12 min while that of cotreated with Sir-Actin and fluo-4 AM were captured at 10-s intervals for 6 min using a confocal scanning microscope (DMi8, Leica, Wetzlar, Germany). The intensity of F-actin area from all Sir-Actin positive cells in a field of recording were included in the statistics, and the intensity of F-actin was normalized to the baseline area or intensity at 0 min. Both tests were repeated in 12 different cultures. ImageJ software (ImageJ 1.46r, NIH) was used to analyze all images.

High Performance Liquid Chromatograph Mass Spectrometer (HPLC-MS). The trisodium citrate was diluted in ACSF at a concentration of 18 mg/mL. The anesthetized mice were injected with trisodium citrate into the CIM at a rate of 1 μL/min for 5 min (5 μL total volume), and 4 h later, the mice were decapitated. 30 mg each of the mice brain tissue, brainstem, thoracic spinal cord, and liver, and 5 mg of the hepatic plexus were homogenized at 4 °C and 60 Hz for 3 min using tissue grinder (Scientz-48L, SCIENTZ, Ningbo, China). The tissue homogenate was dissolved with methanol:acetonitrile:water 1:1:2 (v/v/v) solution, centrifuged at 13,000 rpm, and take the supernatant for detection by LC–MS.

The liquid chromatography system (1260 Infinity, Agilent, Santa Clara, CA) was used to separate the test substance before mass spectrometry. The autosampler was set up at room temperature, and the temperature of column was kept at 30 °C. The flow rate of mobile phase is kept at a uniform rate of 0.5 mL/min, and the volume of injection of all samples is always kept at 10 μL. Chromatographic separation was accomplished on a InfinityLab Poroshell 120 SB-C18 column (100 × 4.6 mm i.d., 2.7 μm; Agilent, Santa Clara, CA), the testing time is unified as 3 min. Mobile phase (acetonitrile:water = 70:30, v/v, 0.1% formic acid) was freshly prepared. To prevent for potential carryover, the ratio of methanol to water is maintained at 1:1, v/v.

A mass spectrometer (6420 Triple Quad LC/MS, Agilent, Santa Clara, CA) equipped with a negative turbo ionspray electrospray ionization source was used. Parameters for mass spectrum detection were set as described below: ion-spray voltage, 3,500 V; gas temperature, 310 °C. Using protonated molecule [M–H]− ion for all analyzes. The quantifier and qualifier process used twin multiple reaction monitoring (MRM) transitions. The quantitative MRM was set at

mass-to-charge ratio (m/z) 191.0 → 111.0. Stock solutions of trisodium citrate were prepared using methanol to final concentrations of 200 mg/ml. Working trisodium citrate solutions were freshly produced before every batch analysis, were prepared in methanol:acetonitrile:water = 1:1:2 (v/v/v) at concentration of 10, 100, 1,000, and 10,000 μg/mL.

Viral Vector and Stereotaxic Injection. AAV2 vector was based on Pet-1 promoter, and also included light-sensitive protein hChR2(H134R) and enhanced green fluorescent protein (eGFP). f1 bacteriophage Origin (f1 ori) and Origin (ori) were used to promote plasmid replication and inverted terminal repeat (ITR) was used to stabilize the structure and promote AAV2 production. Using the Kozak sequence to initiate the expression of the inserted gene, woodchuck posttranscriptional regulatory element (WPRE) to increase the expression of the inserted gene, and bovine growth hormone polyadenylation (bGH polyA) to terminate transcription. Using the ampicillin resistance gene (AmpR) promoter to control AmpR expression to render the AAV2 vector ampicillin-resistant, allowing for ampicillin-specific selection of positive clones (*SI Appendix*, Fig. S3*B*). The AAV2 vector was synthesized at the titer of 1.3×10^{13} V.G./mL by Taitool Bioscience Co., Ltd. The mice were placed on stereotaxic instrument, properly disinfected, and then subjected to scalp incision and skull window opening. Five-fold diluted viral vector was injected into the dorsal raphe nucleus [DRN; Bregma: −4.36 mm, medial–lateral (ML): 0 mm] at 0.2 μL/min for 5 min using a 30G needle. The needle was pulled out 10 min after the end of the injection and the optogenetic fiber was implanted. The 470 nm blue light laser (F-470-HS-OEM, Changchun New Industry Optoelectronic Technology Co. LTD, China) was used to stimulate light-sensitive serotonergic neurons 3 wk after AAV2 vector injection.

Trisodium Citrate Quantification in Tissues. Chromatography data were acquired and analyzed using Agilent MassHunter Workstation Software LC/MS Data Acquisition (version B.07.00, Agilent) and Qualitative Analysis (version B.06.00, Agilent). Using standard curve to calculate the trisodium citrate content in tissue samples, the content of trisodium citrate from different groups was normalized to the content of the control group.

Statistical Analysis. Power analysis and sample size (PASS) 2020 software (NCSS LLC, East Kaysville, UT) was used to estimate the suitable sample number in in vivo and in vitro experiments. One-way ANOVA with the Tukey post hoc test was used for comparisons included more than two groups, unpaired two-tailed *t* test was used for two-group comparisons, GraphPad Prism 9 software (GraphPad Software Inc., La Jolla, CA) and SPSS 24 software (International Business Machines Corp., New York, NY) were used for the above statistics and analyses. All statistical data in the text are presented as the mean ± SEM, the value of significance was set at $P < 0.05$. There was no excluded data and all data were included in the statistical analysis, all statistical analyses were performed by an investigator blinded to the experimental conditions.

Data, Materials, and Software Availability. All study data are included in the article and/or supporting information.

ACKNOWLEDGMENTS. This work was supported by the National Natural Science Foundation of China (32271038 to M.X.), 2024 Liaoning Province Central Guidance Local Science and Technology Development Funding Plan Project ([2024]5-77 to M.X.), and Liaoning Province Science and Technology Plan Joint Program (Foundation) Project ([2023]67-10 to B.L.).

Author affiliations: [a]Department of Forensic Analytical Toxicology, School of Forensic Medicine, China Medical University, Shenyang 110122, China; [b]Liaoning Province Key Laboratory of Forensic Bio-Evidence Sciences, China Medical University, Shenyang 110122, China; [c]China Medical University Centre of Forensic Investigation, Shenyang 110122, China; [d]Department of Molecular Neurosciences, Center for Brain Research, Medical University of Vienna, Vienna 1090, Austria; [e]Department of Neuroscience, Biomedicum, Karolinska Institutet, Solna 17165, Sweden; [f]Faculty of Biology, Medicine and Health, The University of Manchester, Manchester M13 9PL, United Kingdom; [g]Department of Neurosciences, University of the Basque Country, Leioa 48940, Bizkaia, Spain; [h]Department of Stem Cell Biology, State Research Institute Centre for Innovative Medicine, Vilnius LT-01102, Lithuania; and [i]Department of Orthopaedics, The First Hospital, China Medical University, Shenyang 110002, China

1. N. Alperin, A. M. Bagci, S. H. Lee, B. L. Lam, Automated quantitation of spinal CSF volume and measurement of craniospinal CSF redistribution following lumbar withdrawal in idiopathic intracranial hypertension. *Am. J. Neuroradiol.* **37**, 1957–1963 (2016).
2. T. Brinker, E. Stopa, J. Morrison, P. Klinge, A new look at cerebrospinal fluid circulation. *Fluids Barriers CNS* **11**, 10 (2014).
3. J. L. Chazen *et al.*, Automated segmentation of MR imaging to determine normative central nervous system cerebrospinal fluid volumes in healthy volunteers. *Clin. Imaging* **43**, 132–135 (2017).
4. J. Hodel *et al.*, Imaging of the entire cerebrospinal fluid volume with a multistation 3D SPACE MR sequence: Feasibility study in patients with hydrocephalus. *Eur. Radiol.* **23**, 1450–1458 (2013).
5. R. Spector, S. Robert Snodgrass, C. E. Johanson, A balanced view of the cerebrospinal fluid composition and functions: Focus on adult humans. *Exp. Neurol.* **273**, 57–68 (2015).
6. T. O. Wichmann, H. H. Damkier, M. Pedersen, A brief overview of the cerebrospinal fluid system and its implications for brain and spinal cord diseases. *Front. Human Neurosci.* **15**, 737217 (2021).
7. L. M. Hablitz, M. Nedergaard, The glymphatic system: A novel component of fundamental neurobiology. *J. Neurosci.* **41**, 7698–7711 (2021).
8. A. Alpár, M. Benevento, R. A. Romanov, T. Hökfelt, T. Harkany, Hypothalamic cell diversity: Non-neuronal codes for long-distance volume transmission by neuropeptides. *Curr. Opin. Neurobiol.* **56**, 16–23 (2019).
9. A. Verkhratsky, A. Butt, *Neuroglia: Function and Pathology* (Academic Press/Elsevier, 2023), p. 730.
10. A. Alpár *et al.*, Hypothalamic CNTF volume transmission shapes cortical noradrenergic excitability upon acute stress. *EMBO J.* **37** (2018).
11. R. Serra, M. J. Simard, Adherens, tight, and gap junctions in ependymal cells: A systematic review of their contribution to CSF-brain barrier. *Front. Neurol.* **14**, 1092205 (2023).
12. Y. H. Li, S. H. Woo, D. H. Choi, E. H. Cho, Succinate causes α-SMA production through GPR91 activation in hepatic stellate cells. *Biochem. Biophys. Res. Commun.* **463**, 853–858 (2015).
13. J. Li *et al.*, HMGB1-induced autophagy facilitates hepatic stellate cells activation: A new pathway in liver fibrosis. *Clin. Sci. (Lond)* **132**, 1645–1667 (2018).
14. J. H. Ahn *et al.*, Meningeal lymphatic vessels at the skull base drain cerebrospinal fluid. *Nature* **572**, 62–66 (2019).
15. M. E. Pizzo *et al.*, Intrathecal antibody distribution in the rat brain: Surface diffusion, perivascular transport and osmotic enhancement of delivery. *J. Physiol.* **596**, 445–475 (2018).
16. B. M. Miller, I. M. Oderberg, W. Goessling, Hepatic nervous system in development, regeneration, and disease. *Hepatology* 74, 3513–3522 (2021).
17. C. A. Haemmerle, M. I. Nogueira, I. S. Watanabe, The neural elements in the lining of the ventricular-subventricular zone: Making an old story new by high-resolution scanning electron microscopy. *Front. Neuroanat.* **9**, 134 (2015).
18. K. Møllgård, L. Wiklund, Serotoninergic synapses on ependymal and hypendymal cells of the rat subcommissural organ. *J. Neurocytol.* **8**, 445–467 (1979).
19. J. D. Mikkelsen, A. Hay-Schmidt, P. J. Larsen, Central innervation of the rat ependyma and subcommissural organ with special reference to ascending serotoninergic projections from the raphe nuclei. *J. Comp. Neurol.* **384**, 556–568 (1997).
20. K. L. Simpson, T. M. Fisher, B. D. Waterhouse, R. C. Lin, Projection patterns from the raphe nuclear complex to the ependymal wall of the ventricular system in the rat. *J. Comp. Neurol.* **399**, 61–72 (1998).
21. P. T. Shah *et al.*, Single-cell transcriptomics and fate mapping of ependymal cells reveals an absence of neural stem cell function. *Cell* **173**, 1045–1057.e1049 (2018).
22. A. R. Murtazina *et al.*, A comparative analysis of CSF and the blood levels of monoamines as neurohormones in rats during ontogenesis. *Acta Nat.* **13**, 89–97 (2021).
23. P. Shang *et al.*, Identification of cerebrospinal fluid and serum metabolomic biomarkers in first episode psychosis patients. *Transl. Psychiatry* **12**, 229 (2022).
24. T. Hendricks, N. Francis, D. Fyodorov, E. S. Deneris, The ETS domain factor Pet-1 is an early and precise marker of central serotonin neurons and interacts with a conserved element in serotonergic genes. *J. Neurosci.* **19**, 10348–10356 (1999).
25. S. Verleysdonk *et al.*, Glycogen metabolism in rat ependymal primary cultures: Regulation by serotonin. *Brain Res.* **1060**, 89–99 (2005).
26. L. Blanchoin, R. Boujemaa-Paterski, C. Sykes, J. Plastino, Actin dynamics, architecture, and mechanics in cell motility. *Physiol. Rev.* **94**, 235–263 (2014).
27. R. A. Romanov *et al.*, Molecular interrogation of hypothalamic organization reveals distinct dopamine neuronal subtypes. *Nat. Neurosci.* **20**, 176–188 (2017).
28. K. Yasui, Y. Hashizume, M. Yoshida, T. Kameyama, G. Sobue, Age-related morphologic changes of the central canal of the human spinal cord. *Acta Neuropathol.* **97**, 253–259 (1999).
29. M. R. Del Bigio, Ependymal cells: Biology and pathology. *Acta Neuropathol.* **119**, 55–73 (2010).
30. A. Verkhratsky, A. Semyanov, R. Zorec, Physiology of astroglial excitability. *Function* **1**, zqaa016 (2020).
31. R. Moriyama *et al.*, In vitro increase in intracellular calcium concentrations induced by low or high extracellular glucose levels in ependymocytes and serotonergic neurons of the rat lower brainstem. *Endocrinology* **145**, 2507–2515 (2004).
32. J. R. Genzen, J. C. Platel, M. E. Rubio, A. Bordey, Ependymal cells along the lateral ventricle express functional P2X(7) receptors. *Purinergic Signal.* **5**, 299–307 (2009).
33. N. Marichal, G. Fabbiani, O. Trujillo-Cenóz, R. E. Russo, Purinergic signalling in a latent stem cell niche of the rat spinal cord. *Purinergic Signal.* **12**, 331–341 (2016).
34. Y. C. Li, W. Z. Bai, T. Hashikawa, Regionally varying F-actin network in the apical cytoplasm of ependymocytes. *Neurosci. Res.* **57**, 522–530 (2007).
35. O. Trujillo-Cenóz *et al.*, The ependymal cell cytoskeleton in the normal and injured spinal cord of mice. *J. Neurosci. Res.* **99**, 2592–2609 (2021).
36. L. Veeraval, C. J. O'Leary, H. M. Cooper, Adherens junctions: Guardians of cortical development. *Front. Cell Dev. Biol.* **8**, 6 (2020).
37. M. Suzuki *et al.*, Strong dependence of hydration state of F-Actin on the bound Mg(2+)/Ca(2+) ions. *J. Phys. Chem. B* **120**, 6917–6928 (2016).
38. H. Strzelecka-Golaszewska, A. Wozniak, T. Hult, U. Lindberg, Effects of the type of divalent cation, Ca^{2+} or Mg^{2+}, bound at the high-affinity site and of the ionic composition of the solution on the structure of F-actin. *Biochem. J.* **316**, 713–721 (1996).
39. K. Chen *et al.*, A unique NLRC4 receptor from echinoderms mediates Vibrio phagocytosis via rearrangement of the cytoskeleton and polymerization of F-actin. *PLoS Pathog.* **17**, e1010145 (2021).

40. L. Zheng *et al.*, Ryanodine receptor calcium release channels in trophoblasts and their role in cell migration. *Biochim. Biophys. Acta, Mol. Cell Res.* **1869**, 119139 (2022).
41. N. E. Fultz *et al.*, Coupled electrophysiological, hemodynamic, and cerebrospinal fluid oscillations in human sleep. *Science* **366**, 628–631 (2019).
42. J. B. Brierley, The penetration of particulate matter from the cerebrospinal fluid into the spinal ganglia, peripheral nerves, and perivascular spaces of the central nervous system. *J Neurol. Neurosurg. Psychiatry* **13**, 203–215 (1950).
43. M. Johnston, D. Armstrong, L. Koh, Possible role of the cavernous sinus veins in cerebrospinal fluid absorption. *Cerebrospinal Fluid Res.* **4**, 3 (2007).
44. K. Bechter, The peripheral cerebrospinal fluid outflow pathway—Physiology and pathophysiology of CSF recirculation: A review and hypothesis. *Neurol. Psychiatry. Brain Res.* **17**, 51–66 (2011).
45. S. T. Proulx, Cerebrospinal fluid outflow: A review of the historical and contemporary evidence for arachnoid villi, perineural routes, and dural lymphatics. *Cell. Mol. Life Sci.* **78**, 2429–2457 (2021).
46. D. Raper, A. Louveau, J. Kipnis, How do meningeal lymphatic vessels drain the CNS? *Trends Neurosci.* **39**, 581–586 (2016).
47. K. Møllgård *et al.*, A mesothelium divides the subarachnoid space into functional compartments. *Science* **379**, 84–88 (2023).
48. J. H. Yoon *et al.*, Nasopharyngeal lymphatic plexus is a hub for cerebrospinal fluid drainage. *Nature* **625**, 768–777 (2024).
49. L. Xie *et al.*, Sleep drives metabolite clearance from the adult brain. *Science* **342**, 373–377 (2013).
50. H. Mestre *et al.*, Cerebrospinal fluid influx drives acute ischemic tissue swelling. *Science* **367**, eaax7171 (2020).
51. B. Fricke, K. H. Andres, M. Von Düring, Nerve fibers innervating the cranial and spinal meninges: Morphology of nerve fiber terminals and their structural integration. *Microsc. Res. Tech.* **53**, 96–105 (2001).
52. X. Li *et al.*, A novel murine model of mania. *Mol. Psychiatry* **28**, 3044–3054 (2023).
53. S. Liang *et al.*, Iron aggravates the depressive phenotype of stressed mice by compromising the glymphatic system. *Neurosc. Bull.* **36**, 1542–1546 (2020).
54. M. Xia *et al.*, The ameliorative effect of fluoxetine on neuroinflammation induced by sleep deprivation. *J. Neurochem.* **146**, 63–75 (2018).
55. C. Prothmann, J. Wellard, J. Berger, B. Hamprecht, S. Verleysdonk, Primary cultures as a model for studying ependymal functions: Glycogen metabolism in ependymal cells. *Brain Res.* **920**, 74–83 (2001).
56. B. Li, S. Zhang, H. Zhang, L. Hertz, L. Peng, Fluoxetine affects GluK2 editing, glutamate-evoked Ca(2+) influx and extracellular signal-regulated kinase phosphorylation in mouse astrocytes. *J. Psychiatry Neurosci.* **36**, 322–338 (2011).
57. T. Hirao *et al.*, Transforming growth factor-β1 and bone morphogenetic protein-2 inhibit differentiation into mature ependymal multiciliated cells. *Biol. Pharm. Bull.* **46**, 111–122 (2023).
58. W. Guan *et al.*, Iron induces two distinct Ca(2+) signalling cascades in astrocytes. *Commun. Biol.* **4**, 525 (2021).